Strain Rate-Dependent Deformation Mechanisms in CMSX-4 at 800 °C: Insights from Full-Field Optical Extensometry

MELVIN Z. MIQUEL, SATOSHI UTADA, YUANBO T. TANG, ATSUSHI SATO, NICK R. GREEN, and ROGER C. REED

The deformation behaviour of a Ni-base single crystal superalloy is studied using a multiscale approach incorporating a recently developed videography arrangement, allowing for full-field digital image correlation. Single crystal CMSX-4 in the ⟨001⟩ orientation was used to obtain a significant tensile dataset spanning temperatures from ambient to 900 °C and strain rates from 10^{-1} to 10^{-5} s^{-1}. A multiscale approach was applied particularly to three strain rates at 800 °C, to determine transitions in the deformation mechanisms. It is demonstrated that the macroscopic deformation patterns correlate well with microscopic observations; moreover, the full-field strain mapping offers useful insights into the underlying shear and slip events. The strain rate sensitivity was particularly pronounced in the regime emphasised and evidence is presented for transitions in deformation mechanism within a single test as deformation proceeds.

https://doi.org/10.1007/s11661-025-08098-4

I. INTRODUCTION

THE deformation behaviour of single crystal superalloys, such as CMSX-4, is governed by an interplay between effects of temperature, stress state, and strain rate. Whilst the creep, tensile, and fatigue behaviours are often treated as distinct mechanical responses, the underlying deformation mechanisms—exemplified by dislocation-precipitate interactions—are often shared across testing conditions with many common features. In particular, the γ/γ' microstructure of these alloys gives rise to temperature and strain rate-dependent transitions in plasticity, governed by the complex nature of dislocation motion.[1,2]

Thus at low temperatures (< 600 °C), significant plastic deformation is most closely associated with shearing of γ' via coupled pairs of dislocations by separated anti-phase boundaries (APBs)—only limited strain rate sensitivity results.[3] At higher temperatures (> 850 °C), thermally activated processes such as dislocation climb within γ and γ' bypassing (via unpaired $a/2\langle 011\rangle$ dislocations) become rate-controlling, resulting in time-dependent creep deformation.[4] But between these limits lies an intermediate regime where competition between the deformation mechanisms, such as microtwinning[5] and stacking faults,[6] are pronounced. More emphasis needs to be placed on the effects occurring here. While conventional creep testing has traditionally been used to characterise high-temperature deformation, recent studies[7,8] have shown that tensile testing at varying strain rates can be helpful in providing insights into the active deformation modes.

In this study, we employ strain rate sensitivity testing on CMSX-4 to investigate the transition between tensile-like and creep-like deformation. By coupling this with full-field optical strain mapping, we link macroscopic strain behaviour to microscopic deformation patterns. This approach enables identification of the dominant deformation mechanisms as a function of strain rate and offers a high-resolution framework for understanding how dislocations respond to local microstructural and thermal conditions.

MELVIN Z. MIQUEL is with the Department of Materials, University of Oxford, Parks Road, OX1 3PH, Oxford, UK. Contact e-mail: melvin.miquel@materials.ox.ac.uk. SATOSHI UTADA is with the Department of Materials, University of Oxford and also with the Research Center for Structural Materials, National Institute for Materials Science, 1-2-1 Sengen, Tsukuba, 305-0047, Japan. YUANBO T. TANG is with the Department of Materials, University of Oxford and also with the School of Metallurgy and Materials, University of Birmingham, Elms Road, Birmingham, B15 2TT, UK. ATSUSHI SATO and NICK R. GREEN are with the High Temperature Research Centre, University of Birmingham, Airfield Drive, Coventry, CV7 9BF, UK. ROGER C. REED is with the Department of Materials, University of Oxford and also with the High Temperature Research Centre, University of Birmingham.
Manuscript submitted September 28, 2025; accepted December 23, 2025.

Article published online January 15, 2026

II. EXPERIMENTAL DETAILS

A. *Material and Specimen Preparation*

The material studied is CMSX-4, a second-generation single crystal superalloy with composition (in wt pct): 9.6 Co, 6.5 Cr, 0.6 Mo, 6.4 W, 6.5 Ta, 3.0 Re, 5.6 Al, 1.0 Ti, 0.1 Hf, balance Ni, supplied by the High Temperature Research Centre (HTRC), a joint collaboration between the University of Birmingham and Rolls-Royce plc. The material was supplied as bars with diameters of approximately 14 mm and lengths of approximately 230 mm, in a condition consistent with a solution and single ageing heat treatment, without a second ageing step. Specimens were subsequently machined to a cylindrical dogbone-style geometry with a 6 mm gauge length and 3.5 mm gauge diameter. The specimens were machined to maintain the ⟨001⟩ crystallographic orientation of their parent bars. The exact orientation of the bars was measured using back Laue approaches, confirming that all specimens tested were within 3 deg misorientation from ⟨001⟩. Surfaces were left with a lathe finish and prepared for DIC by applying a fine speckle pattern onto the surface with a coat of VHT thermal-resistant white primer followed by VHT black spray paint applied in a light misting technique.

B. *Mechanical Testing*

In this work, in excess of 40 tensile tests were conducted to failure. Temperatures from room temperature to 900 °C and constant strain rates from 10^{-1} to 10^{-5} s^{-1} were used, as summarised in Table I.

Uniaxial tensile tests were conducted, using an Instron 8862 servo-electric testing machine equipped with a 100 kN load cell. Temperature control was achieved using a Severn Thermal Solutions SF2232 three-zone rapid heating resistance wire element split furnace, operated in air with N-type thermocouple feedback control. Before loading, the specimens were soaked at temperature for 30 minutes to ensure thermal equilibrium. Temperature uniformity within the gauge section was maintained to within ± 1 °C throughout the testing.

Each test was conducted to failure to capture the complete macroscopic deformation evolution from initial loading through to final fracture, thus enabling correlation of strain patterns with different stages of the deformation process. No physical extensometers were employed; instead, all strain measurements were captured optically using a recently developed four-camera digital image correlation (DIC) system[9] including the Imetrum Flexi Video Gauge software. The system employs four cameras positioned at 90 deg intervals around the specimen, providing complete circumferential strain field measurement. Experiments were carried out at acquisition rates from 1 to 100 Hz depending on strain rate, and an exposure time of 10,000 μs. The spatial resolution of the cameras is 17 to 25 μm/px and the cameras are synchronised by the Imetrum software. Stress-strain curves were derived from force (from the machine) and extensometry data (from the DIC trackers placed on the specimen surface).

C. *DIC Analysis*

Full-field DIC analysis was performed using the open-source Ncorr V1.2 software package[10] to quantify the macroscopic strain distribution across the specimen gauge sections. A subset radius of 13 and subset spacing of 1 was used as DIC parameters and this was kept fixed for all test recordings. The four synchronised video recordings, for a given experiment, were reduced to a representative stack of 400 frames per camera by selecting corresponding frames at identical time intervals across all cameras. Using this methodology any individual frame can be stitched with its neighbour camera frame, by using common patterns from the speckling, to create a 2D full-field strain map which enables identification of strain localisation patterns and heterogeneous deformation behaviour. This strain mapping provided context for subsequent microscopic analyses by identifying regions of interest where localised deformation had occurred, thereby guiding the selection of areas for microstructural examination.

D. *SEM Analysis*

Fractographic analysis was performed using a Zeiss Merlin scanning electron microscope to identify the dominant failure modes and assess their correlation with the applied strain rate conditions. Following fractography, specimens were mechanically polished to a 1 μm finish. Final surface preparation involved 30 minutes of polishing using an OPS solution. Microstructural characterisation was carried out using scanning electron microscopy with electron channelling contrast imaging (SEM-ECCI). Fractographic imaging was conducted at an accelerating voltage (EHT) of 20 kV with a probe current of 1 nA. SEM-ECCI was performed under the same conditions, with a working distance of approximately 7 mm.

III. RESULTS

Results from the uniaxial tensile curves are given as a strain rate-temperature yield strength map in Figure 1(a). At temperatures equal to and below 650 °C, only minimal strain rate dependence was found, with the yield strength remaining relatively constant across all strain rates tested. Between 700 °C and 750 °C, the yield strength started to increase, and a strain rate sensitivity arose.[11] At 800 °C the strain rate sensitivity became significantly pronounced, with yield strength variations exceeding 300 MPa across the strain rate spectrum employed. A summary of the mechanical data extracted for all the completed test conditions can be found in Table II.

Moreover, the anomalous yield regime, which is typical of single crystal Ni-based superalloys,[12,13] is clear and characterised by a strength which increases with temperature. But the temperature with the highest

Table I. Summary of Test Conditions Used in the Study

Temp (°C)→ Strain Rate (s^{-1}) ↓	RT	100	200	300	400	500	600	650	700	750	800	850	900
1×10^{-1}	✔							✔	✔	✔	✔	✔	✔
1×10^{-2}	✔							✔	✔	✔	✔	✔	✔
1×10^{-3}	✔	✔	✔	✔	✔	✔	✔	✔	✔	✔	✔	✔	✔
1×10^{-4}	✔							✔	✔	✔	✔	✔	✔
1×10^{-5}	✔							✔	✔	✔	✔	✔	✔

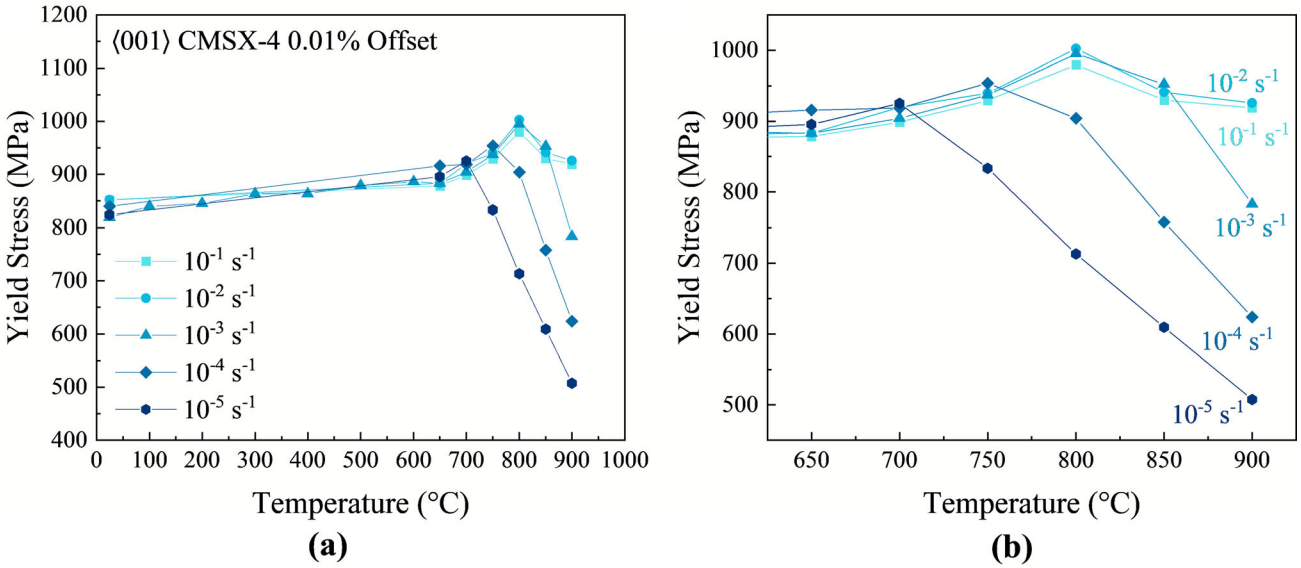

Fig. 1—Sensitivity of the yield stress, calculated using a 0.01 pct offset, to temperature and strain rate for ⟨001⟩ oriented CMSX-4 tested in uniaxial tension: (*a*) full range of temperatures, (*b*) blow-up of anomalous yield regime.

strength within the anomalous regime is found to depend strongly on the strain rate applied.[14–16] As illustrated by Figure 1(b), the strongest temperatures for each strain rate going from the slowest rate of 10^{-5} s^{-1} to the fastest rate of 10^{-1} s^{-1} are approximately 700 °C, 750 °C, 800 °C, 800 °C, and 800 °C, respectively.

To enable a focussed mechanistic analysis, we restricted the present study to three strain rates (10^{-2}, 10^{-3}, and 10^{-4} s^{-1}) at 800 °C. This temperature lies in the transitional regime for CMSX-4, where the influence of strain rate on deformation behaviour becomes particularly pronounced. The chosen rates span two orders of magnitude, capturing high-, intermediate-, and low-rate behaviour while remaining experimentally manageable. Preliminary analysis indicated that 10^{-4} s^{-1} exhibited markedly different work-hardening, strain localisation, and symmetry transition behaviour compared to 10^{-2} and 10^{-3} s^{-1}, making it an ideal case for detailed comparison.

A. *Macroscopic Deformation Behaviour*

Representative engineering stress-strain curves at 800 °C are shown in Figure 2(a). Each curve exhibits unique post-yield hardening behaviour, consistent with differing thermally activated diffusion and dislocation processes.[8,17] The 0.01 pct offset yield stress varies greatly between the lower rate (10^{-4} s^{-1}) and the two higher rates (10^{-2} and 10^{-3} s^{-1}). At the lower rate of 10^{-4} s^{-1}, yield occurs at approximately 900 MPa compared to approximately 1000 MPa at the higher rates, with 10^{-2} s^{-1} being marginally stronger by about 5 MPa.

The consistency of elastic moduli across strain rates (100 to 105 GPa) confirms that the material's fundamental elastic properties remain constant, indicating that the observed rate sensitivity originates from plastic deformation mechanisms rather than elastic anisotropy effects. The four-camera measurement system is shown to provide good repeatability. Yield strength values were calculated from each camera for each test, with standard deviations in stress measurements across the four cameras typically less than 10 MPa.

True stress–strain curves, Figure 2(b), were obtained from the engineering curves using the standard conversion, $\sigma_{true} = \sigma_{eng}(1 + \varepsilon_{eng})$ and $\varepsilon_{true} = \ln(1 + \varepsilon_{eng})$. This approach is typically invalidated once necking begins; however, the advantage of optical extensometry is that it can be confirmed that all tests exhibited minimal necking prior to failure, even at the lowest strain rate.

Table II. Summary of Key Mechanical Data for All Tensile Experiments

Temperature (°C)	Strain Rate (s^{-1})	Orientation θ (Deg)	Elastic Modulus (GPa)	Failure Strain (Pct)	Offset Yield Strength (MPa)		
					0.01 Pct	0.10 Pct	0.20 Pct
25	10^{-1}	1.7	131	9	852	899	920
	10^{-2}	1.7	139	8	852	893	912
	10^{-3}	1.7	139	8	820	894	912
	10^{-4}	1.7	142	6	840	898	916
	10^{-5}	1.7	142	9	824	889	905
100	10^{-3}	2.8	127	10	840	881	895
200	10^{-3}	2.8	121	6	845	877	897
300	10^{-3}	2.8	122	4	863	894	916
400	10^{-3}	2.8	118	3	863	917	935
500	10^{-3}	2.8	113	4	879	906	920
600	10^{-3}	2.8	108	3	886	924	947
650	10^{-1}	2.4	114	2	879	908	932
	10^{-2}	2.4	111	3	883	914	929
	10^{-3}	2.4	112	6	883	915	930
	10^{-4}	2.4	113	12	916	944	960
	10^{-5}	2.4	105	16	896	931	947
700	10^{-1}	2.4	110	3	899	958	981
	10^{-2}	2.4	109	4.5	919	958	978
	10^{-3}	2.4	111	11	904	940	956
	10^{-4}	2.4	109	16	919	951	968
	10^{-5}	2.4	105	27	925	957	977
750	10^{-1}	1.4	104	4.5	929	970	993
	10^{-2}	1.4	103	7	940	981	1005
	10^{-3}	1.4	106	12	937	988	1008
	10^{-4}	1.4	101	27	954	990	1012
	10^{-5}	1.4	104	25	833	887	900
800	10^{-1}	0.8	102	8	980	1020	1048
	10^{-2}	0.8	101	11	1002	1039	1071
	10^{-3}	0.8	106	19	995	1035	1077
	10^{-4}	0.8	99	25	904	946	963
	10^{-5}	0.8	99	24	713	748	752
850	10^{-1}	2.7	98	9	930	978	1016
	10^{-2}	2.7	98	17	941	1003	1065
	10^{-3}	2.7	95	31	952	1059	1102
	10^{-4}	2.7	95	27	758	802	815
	10^{-5}	2.7	95	24	609	630	642
900	10^{-1}	2.7	95	14	919	1002	1106
	10^{-2}	2.7	92	28	926	1094	1156
	10^{-3}	2.7	91	24	783	876	900
	10^{-4}	2.7	91	27	624	676	695
	10^{-5}	2.7	89	28	508	557	575

The near-uniform axial strain distribution supports the use of this conversion, ensuring that the calculated true stress and strain values are representative of the bulk material response rather than localised deformation.

B. *Strain Field Evolution and Localisation Patterns*

Before examining the specific strain rate conditions, it is important to clarify the terminology used to describe the observed deformation patterns. Figure 3 provides a schematic illustration of the symmetry concepts referenced throughout this section and what follows. Twofold symmetry [Figure 3(a)] corresponds to a deformation pattern in which strain localisation develops along two opposing regions of the specimen circumference. When the cyclindrical surface is ''unwrapped'' into a 0 to 360 deg map, this localised band appears as a peak and trough separated by 180 deg. This produces a single dominant axis of symmetry around the circumference, consistent with deformation that favours

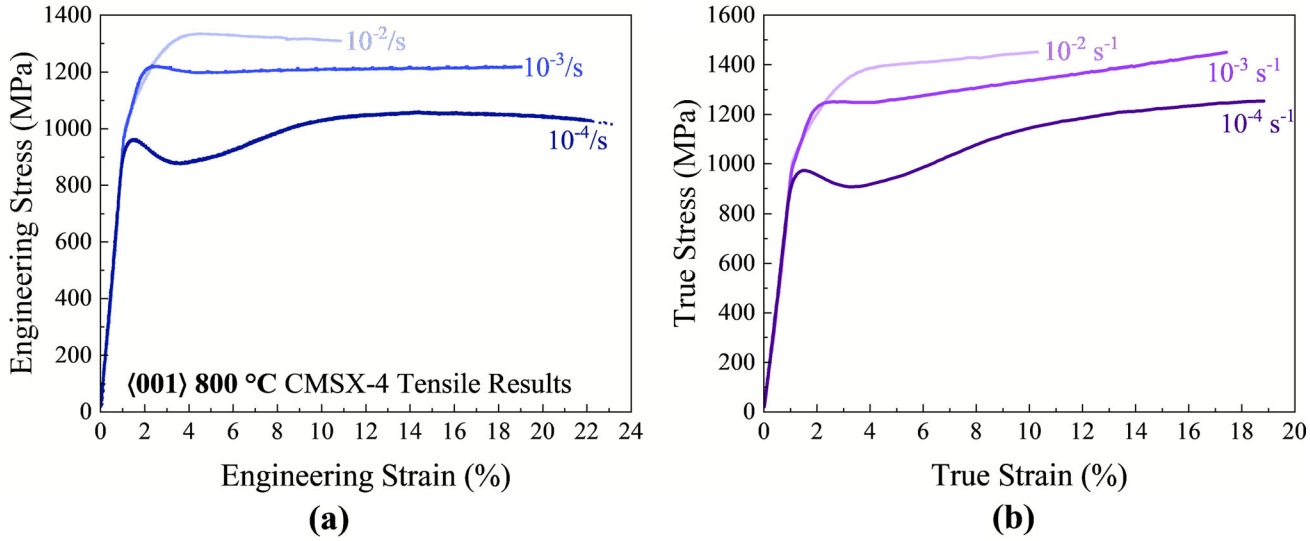

Fig. 2—Experimental tensile test stress-strain curves of ⟨001⟩ oriented CMSX-4 tested at 800 °C at three different strain rates (10^{-2}, 10^{-3}, and 10^{-4} s^{-1}); (*a*) Engineering, and (*b*) True.

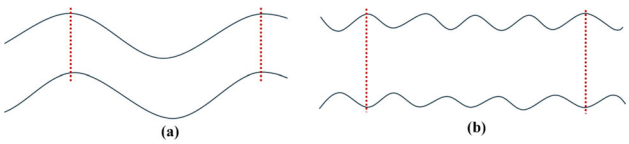

Fig. 3—Schematic curves of how different forms of symmetry appear in 2D full-field strain maps, (*a*) twofold and (*b*) fourfold.

one primary plane or axis. By contrast, fourfold symmetry [Figure 3(b)] reflects a deformation pattern that repeats every 90 deg. When the circumference is laid out from 0 to 360 deg, four evenly spaced localisation peaks emerge, each separated by 90 deg. This indicates that the strain field contains four equivalent preferential directions around the loading axis, producing a pattern with four rotational symmetry elements.

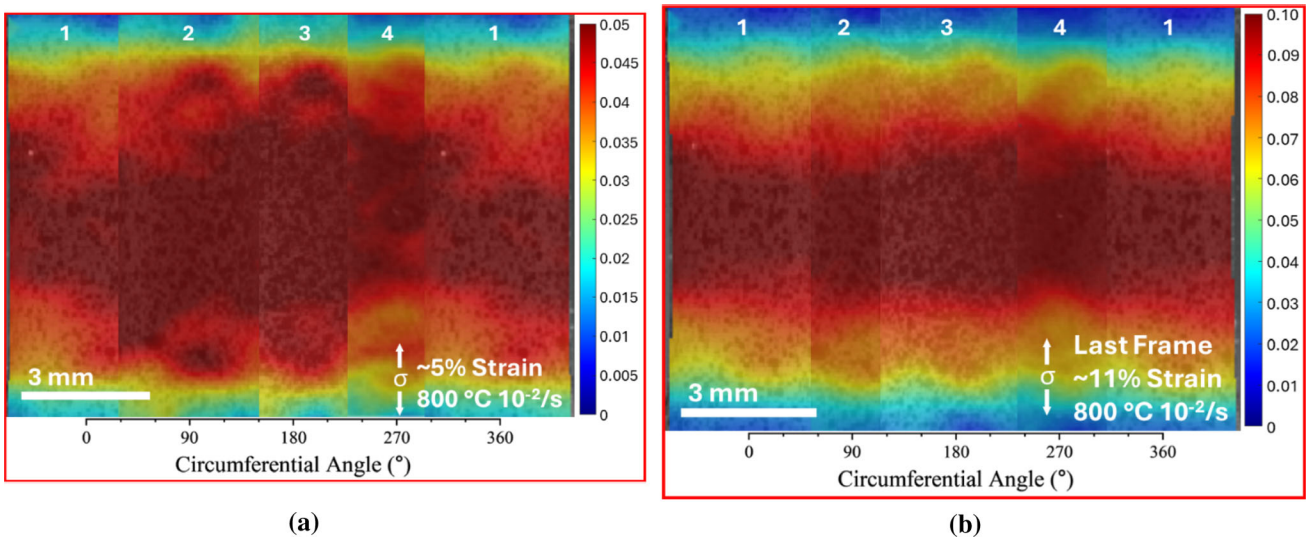

Fig. 4—Surface strain maps along the tensile direction, ε_{zz}, of ⟨001⟩ oriented CMSX-4 tested at 800 °C and 10^{-2} s^{-1} (*a*) 5 pct, and (*b*) 11 pct. Numbers atop indicate the camera identity.

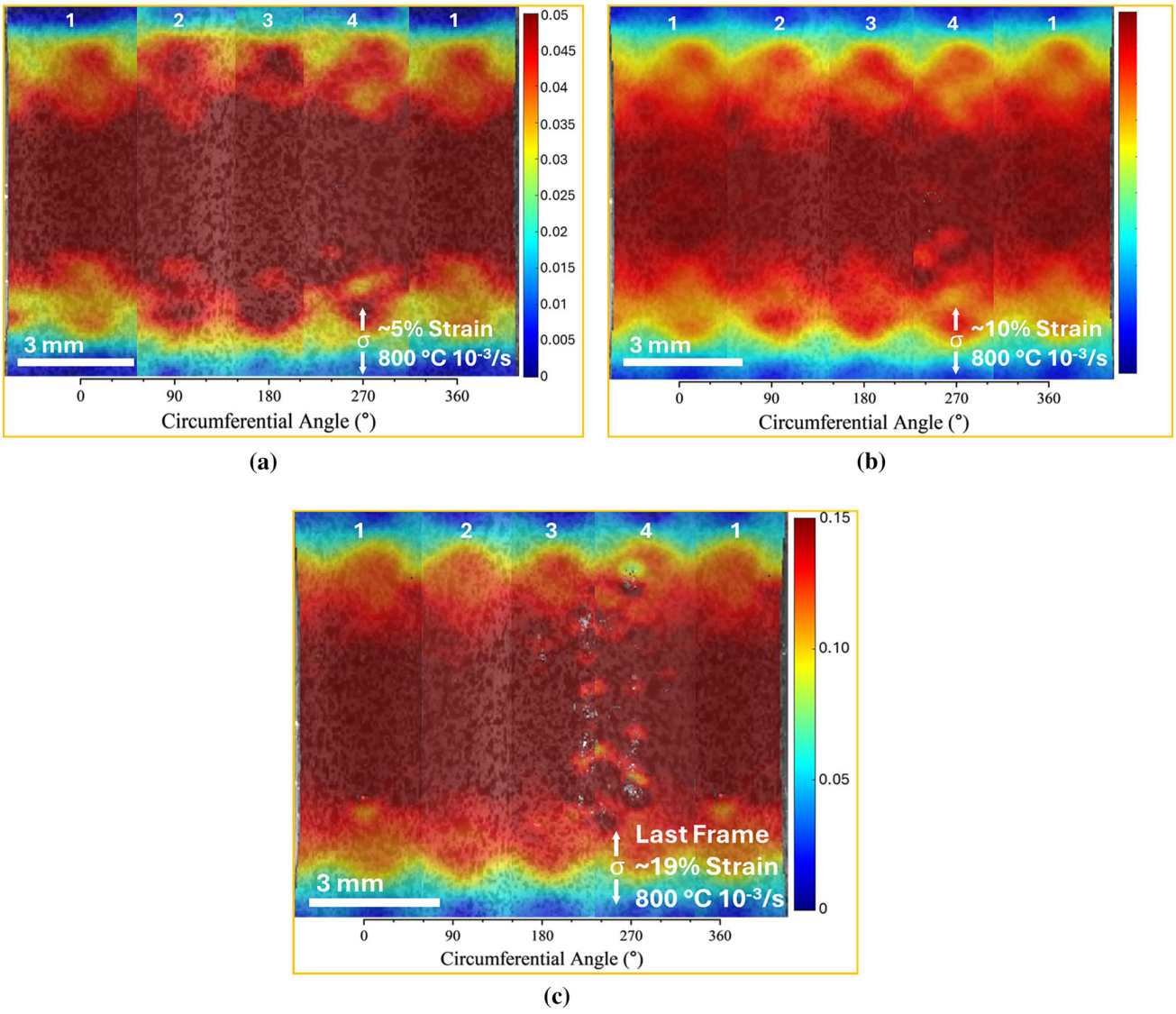

Fig. 5—Surface strain maps along the tensile direction, ε_{zz}, of ⟨001⟩ oriented CMSX-4 tested at 800 °C and 10^{-3} s^{-1} (*a*) 5 pct global strain, (*b*) 10 pct, and (*c*) 19 pct. Numbers atop indicate the camera identity.

At the highest strain rate tested (10^{-2} s^{-1}), deformation was found to initiate uniformly across the gauge section with gradual strain localisation. At 5 pct global strain [Figure 4(a)], localisation begins to become apparent, with a weak fourfold symmetry emerging. Two of the four potential {111} slip systems are dominating (seen in cameras 2 and 3). Figure 4(b) reveals that before final failure occurs, only a heterogenous strain distribution remains, with what appears to be two dominant slip systems active.

At 10^{-3} s^{-1}, a fourfold symmetry develops by 5 pct global strain [Figure 5(a)] and persists through to failure [Figures 5(b) and (c)]. The strain localisation is crystallographically consistent, indicating balanced activation of the four equivalent {111}⟨110⟩ slip systems in the ⟨001⟩ orientation.

At 10^{-4} s^{-1}, the strain field evolution is markedly different. Initial twofold symmetry is seen at 3.5 pct global strain [Figure 6(a)], followed by a transition to fourfold at 10 pct strain [Figure 6(b)]. By 20 pct global strain [Figure 6(c)] there is heavy localisation onto what appears to be two separate slip systems. By fracture this has localised almost entirely, reverting back to twofold symmetry [Figure 6(d)], like that seen in Figure 6(a). Maximum local strains exceed 30 pct highlighting the fact that deformation has become extremely localised.

C. *Fractographic Analysis and Failure Mode Evolution*

At both 10^{-2} s^{-1} [Figure 7(a)] and 10^{-3} s^{-1} [Figure 7(b)], the fracture surfaces are smooth and planar, with minimal evidence of secondary cracking or branching. Higher magnification reveals predominantly cleavage-like features, with limited tearing ridges or small steps, indicative of only limited plastic deformation and a fracture mode characterised by localised shearing. However, at 10^{-3} s^{-1}, the fracture surface shows slightly increased textural complexity and the emergence of

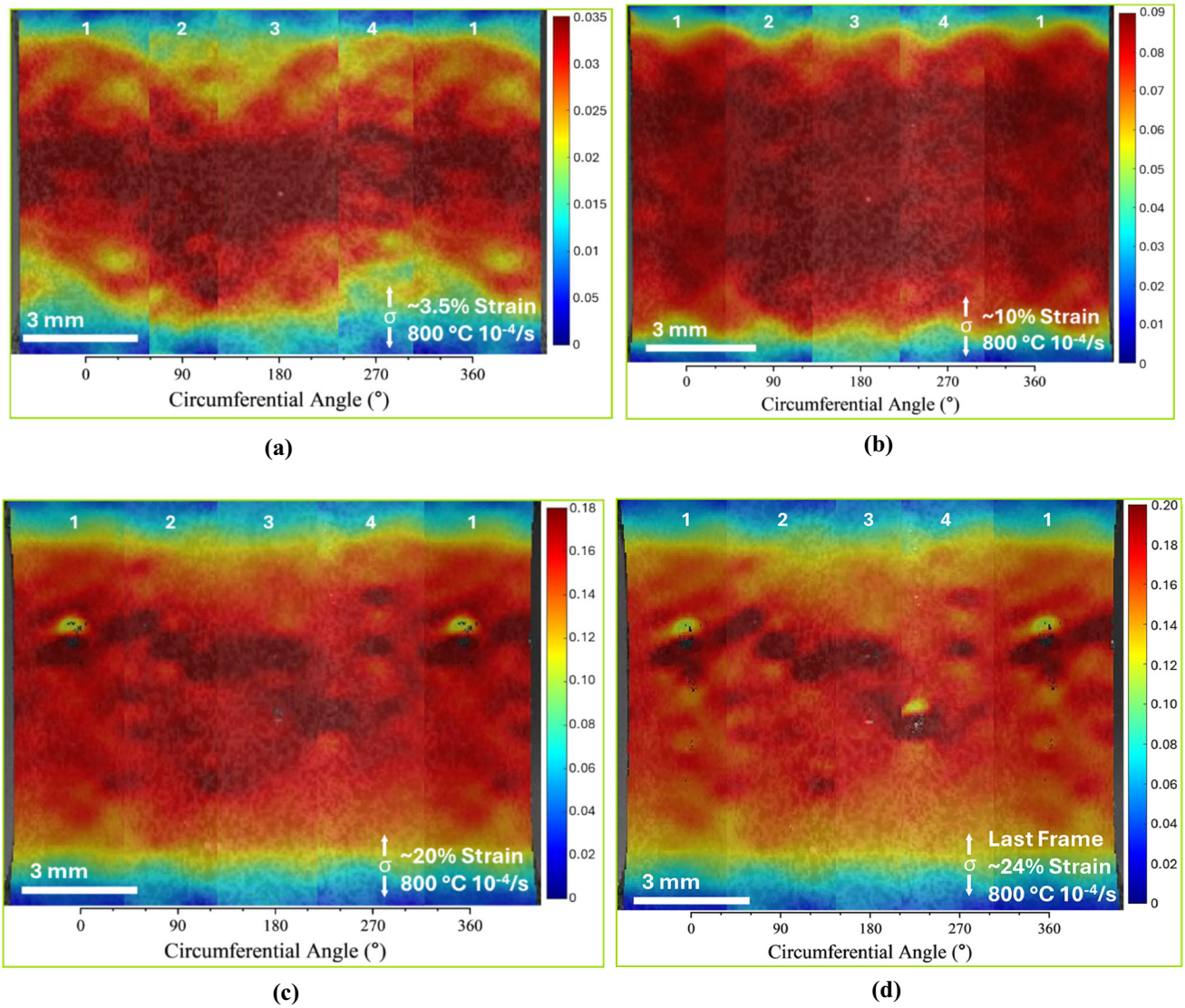

Fig. 6—Surface strain maps along the tensile direction, ε_{zz}, of ⟨001⟩ oriented CMSX-4 tested at 800 °C & 10^{-4} s^{-1} (*a*) 3.5 pct global strain, (*b*) 10 pct, (*c*) 20 pct, and (*d*) 24 pct. Numbers atop indicate the camera identity.

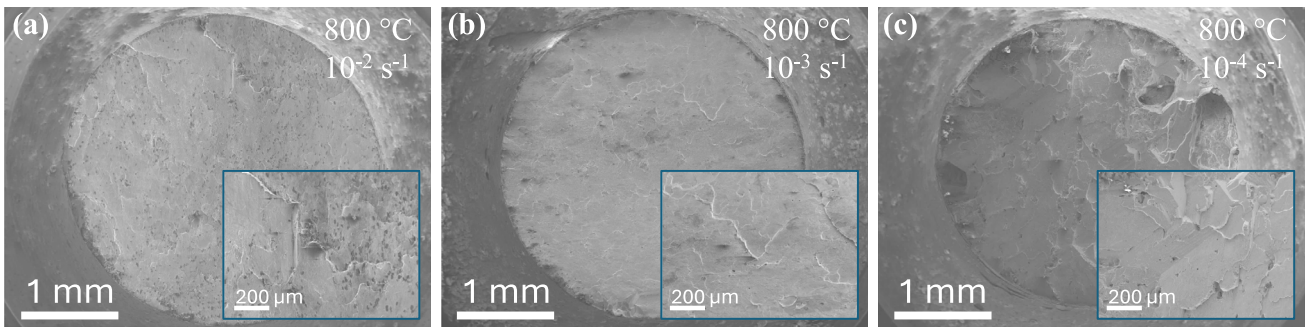

Fig. 7—Fractographs of ⟨001⟩ oriented CMSX-4 tensile specimens tested at 800 °C: (*a*) 10^{-2} s^{-1}, (*b*) 10^{-3} s^{-1}, and (*c*) 10^{-4} s^{-1}.

mixed-mode characteristics, suggesting the onset of further deformation mechanisms. This subtle shift is consistent with the higher strain to failure observed at 10^{-3} s^{-1} (19 pct) compared to 10^{-2} s^{-1} (11 pct), reflecting a transition from rapid, highly localised shear-dominant failure towards more distributed plasticity.

Significant deviations in fracture morphology are observed at the lowest strain rate [10^{-4} s^{-1}, Figure 7(c)], where the fracture surface appears highly

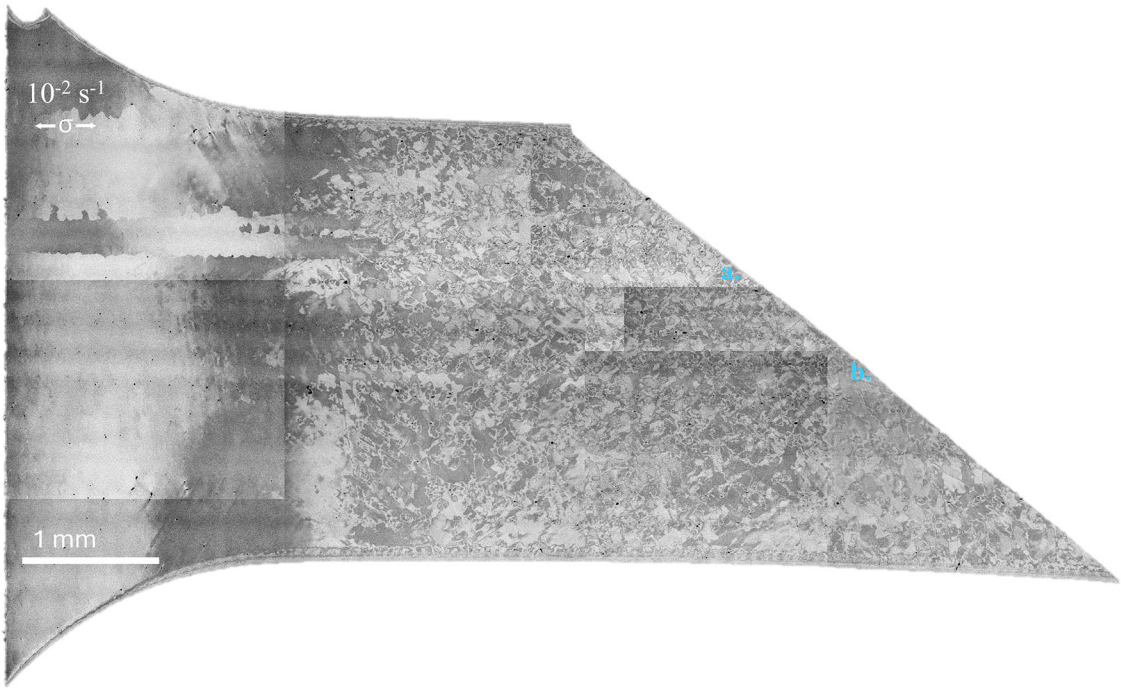

Fig. 8—Stitched SEM-ECCI image of the gauge section, observed near the (110) plane, after failure for the 800 °C/10^{-2} s^{-1} condition.

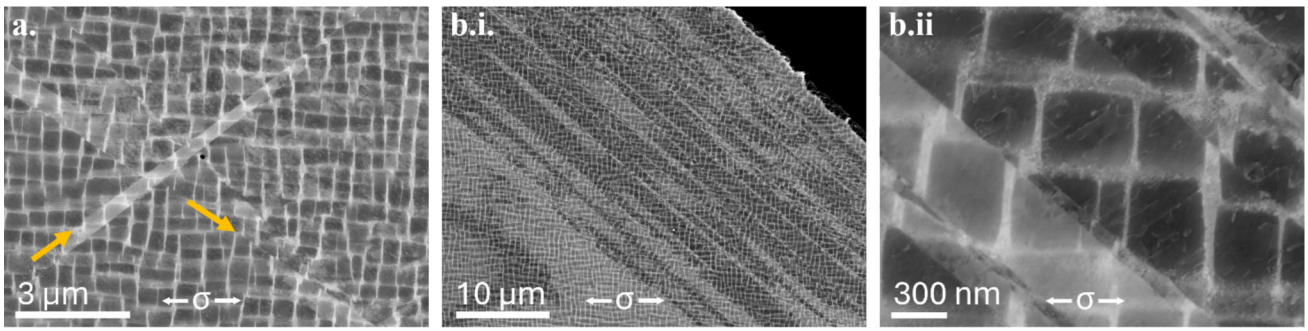

Fig. 9—SEM-ECCI micrographs taken at corresponding locations within Fig. 8: (*a*) opposing shear planes (denoted by orange arrows), (*b*.i) overview of slip bands, and (*b*.ii). higher magnification view of (b.ii) (Color figure online).

irregular and rough, with prominent topographical features, multiple secondary cracks, and appreciable deviations in fracture plane orientation. High-magnification imaging identifies extensive ductile features, including fracture plane deviations and probable evidence of void coalescence/pore branching. Collectively, these microstructural characteristics signify substantial plastic deformation, in contrast to the fracture surfaces at the higher strain rates.

The correlation between fracture morphology and the strain to failure (24 pct) indicates that a decreasing strain rate activates creep-like mechanisms of deformation and damage evolution, resulting in a marked transition from a shear-dominated fracture mode to a ductile failure regime involving more homogeneous plasticity.

D. *Microscopic Deformation Analysis and Slip System Evolution*

Microscopic analysis, via SEM-ECCI, of longitudinal sections taken post-mortem (Figures 8, 10, and 12) reveal significant differences in the extent and nature of slip activity across strain rates. At both 10^{-2} and 10^{-3} s^{-1}, the deformation is characterised by extensive slip banding [Figures 9(b.i) and 10(a)], with pronounced slip induced shearing of the γ' precipitates near the fracture surface [Figure 9(b.ii)]. The density of slip traces is high, and their orientation suggests activation of multiple {111} slip planes [Figures 9(a) and 11(b)].[18,19] In both conditions, the heavy shearing observed near the fracture surface appears to dominate the local deformation. While some isolated dislocations are observed cutting through γ' precipitates, these are sparse and

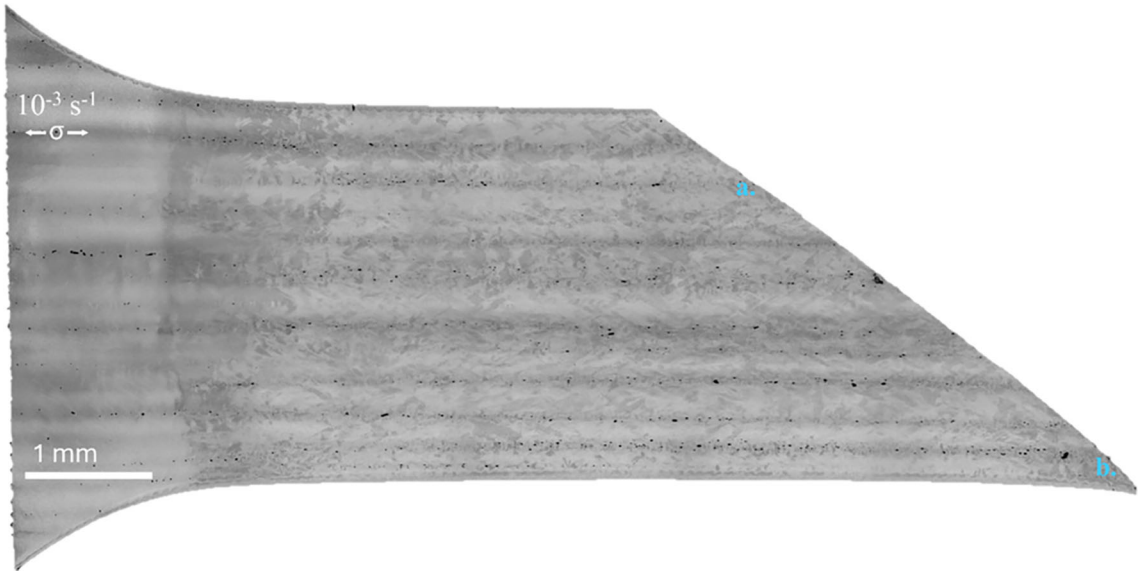

Fig. 10—Stitched SEM-ECCI image of the gauge section, observed near the (110) plane, after failure for the 800 °C/10^{-3} s^{-1} condition.

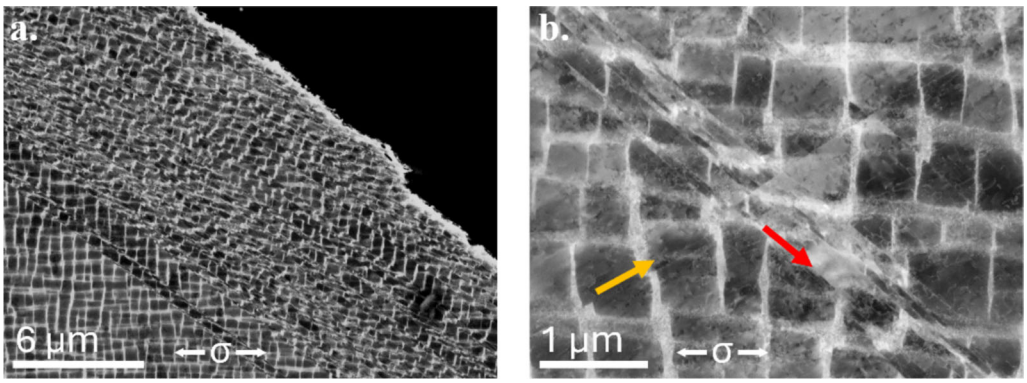

Fig. 11—SEM-ECCI micrographs taken at corresponding locations within Fig. 10: (*a*) showing slip bands, and (*b*) intersecting slip bands where arrows correspond to the primary shear plane (in red) and the secondary shear plane (in orange) (Color figure online).

secondary in nature compared to the overwhelming prevalence of planar slip (Figure 12).

In contrast, the 10^{-4} s^{-1} condition displays less intense slip activity near the fracture surface. Figure 13(b), which is taken near the fracture surface, shows slip traces along multiple {111} planes, but the overall density of slip bands is significantly lower compared to the higher strain rate cases (10^{-2} and 10^{-3} s^{-1}). Moreover, slip induced shearing of the γ' precipitates is much more limited. Alternative thermally activated deformation mechanisms, such as the extended stacking fault shown in Figure 13(a), are weakly evidenced in the current imaging. This reduction in slip activity correlates with the delayed work-hardening and strain localisation behaviour observed in the full-field strain maps, suggesting a transition in the dominant deformation mechanisms as the strain rate decreases. Figure 13(c) shows secondary cracks propagating from a surface crack, strengthening the evidence seen from fractography that the failure is following a much more tortuous path at the lower strain rate.

IV. DISCUSSION

A. *Strain Rate-Dependent Deformation Mechanisms*

The results demonstrate a clear transition in deformation mechanisms at 800 °C as strain rate decreases from 10^{-2} to 10^{-4} s^{-1}, evidenced by both macroscopic strain field evolution and microscopic observations. At higher strain rates (10^{-2} and 10^{-3} s^{-1}), deformation is dominated by conventional slip processes with extensive slip banding and pronounced γ' precipitate shearing (Figures 9 and 11). The high density of slip traces and their orientation confirm activation of multiple {111} slip planes, consistent with anti-phase boundary (APB) shearing mechanisms typical of tensile-like deformation.[20]

In contrast, the 10^{-4} s^{-1} condition exhibits markedly different behaviour. The reduced slip activity near the fracture surface [Figure 13(b)] and the presence of extended stacking faults [Figure 13(a)] indicate that alternative thermally activated mechanisms become accessible at slower strain rates. While stacking faults

Fig. 12—Stitched SEM-ECCI image of the gauge section, observed near the (110) plane, after failure for the 800 °C/10^{-4} s^{-1} condition.

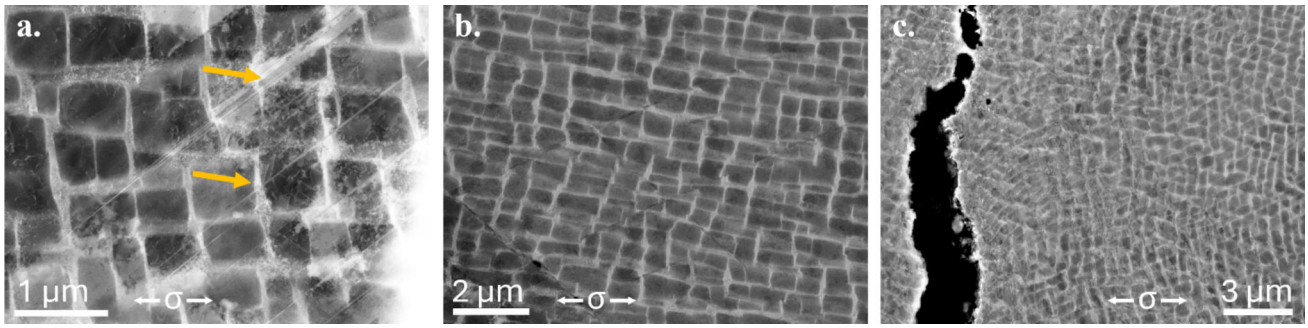

Fig. 13—SEM-ECCI micrographs taken at corresponding locations within Fig. 12: (*a*) showing extended stacking faults denoted by the orange arrows, (*b*) slip traces, and (*c*) a crack near the specimen edge and fracture surface.

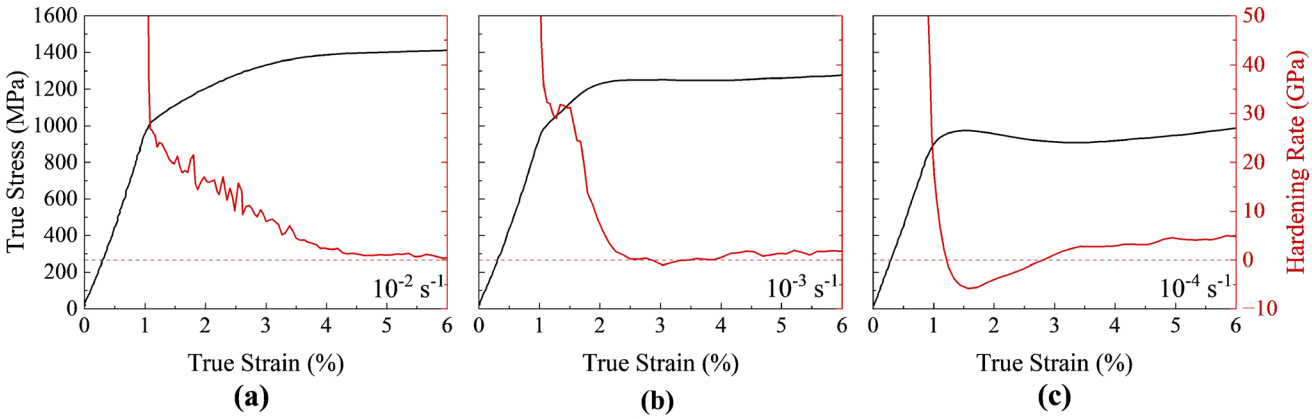

Fig. 14—True stress-strain and hardening rate curves of ⟨001⟩ oriented CMSX-4 tested at 800 °C: (*a*) 10^{-2} s^{-1}, (*b*) 10^{-3} s^{-1}, and (*c*) 10^{-4} s^{-1}.

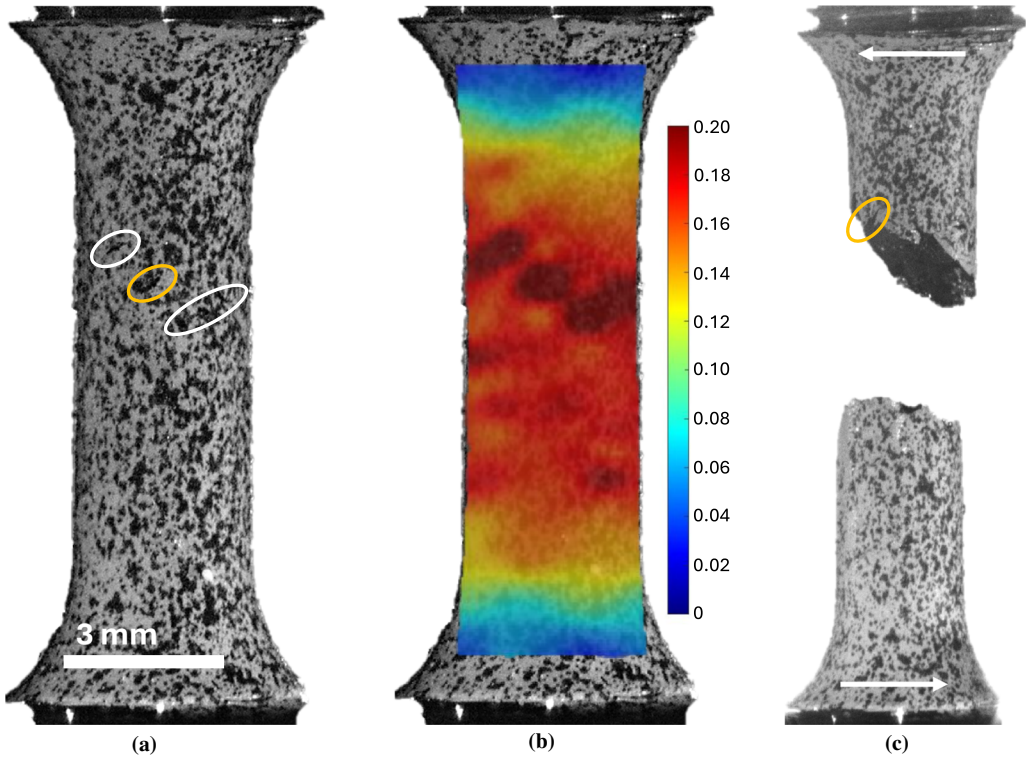

Fig. 15—Final frame (~24 pct strain) from camera 2 of the 10^{-4} s^{-1} test case showing: (*a*) cracks as they appear on the captured frame with ovals highlighting them, (*b*) Ncorr strain mapping (along ε_{zz}) with the cracks concentrating strain, and (*c*) the final fracture with a corresponding oval from frame a. showing the same crack. Arrows in (c) give the direction the specimen rotated in post failure.

are not the dominant deformation mechanism, their presence provides important evidence of partial dislocation motion and represents intermediate steps in various deformation processes, including cross-slip and precipitate shearing. This transition is further supported by the distinct work hardening behaviour: while higher strain rates show immediate onset of strong work hardening (25 to 30 GPa), the 10^{-4} s^{-1} condition displays an initial softening period followed by gradual hardening [Figure 14(c)]. This suggests a shift from APB shearing to stacking fault formation, consistent with the findings of Wang-Koh *et al.*[8]

The fracture morphology corroborates this mechanistic transition. Higher strain rates produce smooth, planar fracture surfaces characteristic of localised shearing, while 10^{-4} s^{-1} exhibits irregular, rough surfaces with evidence of void coalescence and multiple crack paths (Figure 7). The failure behaviour at 10^{-4} s^{-1} is influenced by the interaction between pre-existing casting pores and the time-dependent deformation mechanisms active at low strain rates. While such pores are present in all specimens, see transition radii in Figures 8, 10, and 12, the full-field strain mapping [Figure 15(b)] reveals that their role in damage initiation becomes pronounced only when sufficient time is available for creep-like mechanisms to operate. At higher strain rates (10^{-2} and 10^{-3} s^{-1}), deformation proceeds too rapidly for significant stress concentration and void growth around these defects, resulting in shear-dominated failure on crystallographic planes. In contrast, the 10^{-4} s^{-1} condition provides sufficient time for localised stress relaxation around pores through thermally activated processes, enabling crack nucleation perpendicular to the loading direction [Figures 13(c), 15, and 16]. This represents a fundamental change from shear-dominated to creep-like ductile failure mechanisms involving distributed damage evolution.

B. *Within-Test Deformation Mode Transitions*

It has been well documented that multiple modes of deformation can coexist within a single test.[21–24] These deformation mechanisms can transition within a single test, particularly at higher temperatures and/or slower strain rates where thermally activated mehanisms become significant. The full-field strain mapping enables quantification of when and where these transitions occur, providing insights that would typically require multiple interrupted tests to capture.[8,18,19]

The 10^{-4} s^{-1} specimen provides the clearest evidence of this phenomenon, exhibiting an initial twofold symmetry that transitions to fourfold symmetry, before reverting to twofold symmetry at failure (Figure 6). The twofold symmetry is present at 3 pct true strain. This preferential activation coincides with the softening period, where the hardening rate, $d\sigma/d\varepsilon$, goes negative [Figure 14(c)].

The transition to fourfold symmetry occurs beyond 3 pct true strain, precisely when work hardening begins. At 10 pct global strain, the strain distribution becomes more uniform across all four equivalent {111} slip systems. By 20 pct global strain, extreme localisation

Fig. 16—Stitched SEM-ECCI of ⟨001⟩ oriented CMSX-4 tested at 800 °C/10^{-4} s^{-1} showing cracks growing from pores perpendicular to the loading direction.

develops with maximum local strains reaching 25 to 30 pct while adjacent regions remain at 15 to 20 pct [Figure 6(c)]. This severe heterogeneity precedes the final reversion to twofold symmetry at failure (24 pct global strain), where the dominant slip system carries local strains exceeding 30 pct [Figure 6(d)].

This evolution directly correlates with the microscopic observations: reduced overall slip density but emergence of alternative mechanisms including stacking faults [Figure 13(a)] and surface crack nucleation from pre-existing pores. The ability to capture these transitions in real time—rather than inferring them from post-mortem analysis, interrupted tests or X-ray tomography[25,26]—demonstrates the power of this correlative approach for understanding mechanism evolution.

C. *Stochastic Fracture Plane Selection in Multiple Slip Systems*

An ideal ⟨001⟩-oriented single crystal of FCC crystallography, such as CMSX-4, would exhibit fourfold rotational symmetry about the loading axis, provided that the deformation is slip dominant and active on all {111} planes.[18,27] This symmetry manifests as deformation features repeating every 90 deg, reflecting the underlying crystallographic symmetry.

Despite all three specimens tested at 800 °C exhibiting a fourfold symmetry, to a varying degree, during respective tests, careful analysis of the full-field strain maps reveals the complexity underlying this seemingly balanced deformation. 10^{-2} and 10^{-3} s^{-1} are of particular interest since before failure they are exhibiting fourfold symmetry, yet they fail on a single plane.

Analysing 10^{-2} s^{-1} through a single camera, in this case camera 2, by adjusting the scale [Figure 17(b)] from

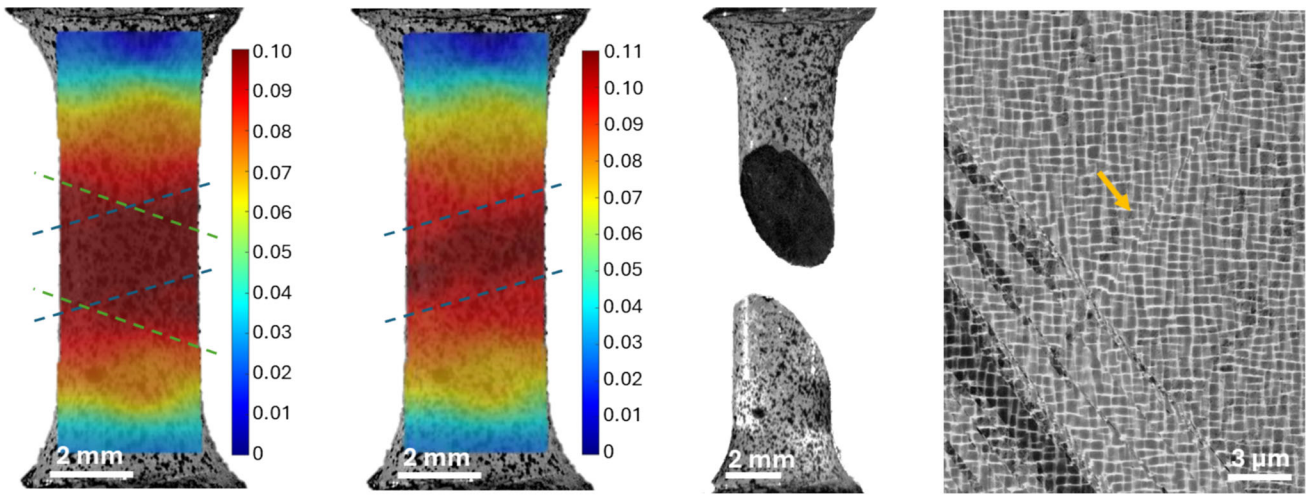

Fig. 17—Final frame before fracture for the 10^{-2} s^{-1} condition showing: (*a*) and (*b*). two active planes, with different colour contour scales revealing (a) both planes and (b) the dominant plane, (*c*) the fracture as seen from the same camera, and (*d*) the correlative microscopy.

the scale used in [Figures 4(b) and 17(a)] a dominant plane can be identified. However, the critical observation is that this macroscopically dominant slip plane does not correspond to the actual fracture plane observed post failure [Figure 17(c)]. SEM-ECCI [Figure 17(d)] confirms the activation of multiple {111} slip planes. The SEM-ECCI analysis reveals secondary slip plane activity shearing through the primary slip plane [Figure 17(d), orange arrow], demonstrating that while the strain maps correctly identify the most active slip system during bulk deformation, final fracture occurs on a different crystallographic plane. Similar observations were reported in a previous study examining the more anisotropic deformation of ⟨011⟩ oriented SX superalloy.[9] The fracture plane appears to be selected stochastically from the available active slip systems, with most of the local shearing occurring at the immediate point of fracture rather than throughout the deformation history. The strain difference between competing slip systems remains small (~1 pct) up to the point of failure, suggesting that fracture plane selection may be influenced by local microstructural features, stress concentrations, or small crystallographic variations rather than being deterministically controlled by the macroscopic loading history.

The videographic evidence supports this interpretation, showing that final failure appears to occur on a plane different from the one that seemed to dominate development until just before fracture. This stochastic nature of fracture plane selection from multiple active slip systems represents a fundamental aspect of single crystal deformation that can only be captured through real time, full-field monitoring combined with detailed post-mortem analysis.

V. SUMMARY AND CONCLUSIONS

In this study, a multiscale characterisation approach combining macroscopic full-field digital image correlation, fractographic analysis, and microscopic examination through SEM-ECCI has been used to study the tensile deformation behaviour of CMSX-4 across length scales. The following specific conclusions can be drawn:

1. The experimental arrangement has allowed for the capturing of the strong strain rate sensitivity of CMSX-4 up to 900 °C, at which temperature for example the yield strength varies by > 500 MPa across the investigated strain rate range of 10^{-1} to 10^{-5} s^{-1}. The rate dependence first appears at 750 °C.
2. The macroscopic results characterise the anomalous yield behaviour more thoroughly than has been reported so far. It is demonstrated that the temperature corresponding to the highest yield strength is particularly sensitive to the strain rate applied. At the slowest strain rate of 10^{-5} s^{-1} the strongest temperature was 700 °C, whilst for the fastest three strain rates (10^{-3} to 10^{-1}) the strongest temperature was 800 °C.
3. The digital image correlation method employed successfully captured and quantified the macroscopic deformation, including some evidence of transitions in behaviour as a test proceeded to failure. For example, in the case of deformation at 10^{-4} s^{-1}, information in the full-field strain map was seen to transition from a twofold strain distribution to a fourfold one. Additionally, the ability to visualise surface crack nucleation prior to final fracture demonstrates the power of correlative full-field techniques for understanding when defect-tolerant design transitions to defect-sensitive behaviour.
4. Microscopic investigations utilising SEM-ECCI demonstrated strong correlation with macroscopic full-field strain mapping across all strain rate conditions, validating the strain maps as accurate predictors of active deformation mechanisms. At higher strain rates (10^{-2} and 10^{-3} s^{-1}), fourfold symmetry in strain maps correlated with extensive slip banding on multiple {111} planes, while the 10^{-4} s^{-1} condition's reduced slip activity and emergence of stacking faults matched the observed symmetry transitions and alternative deformation mechanisms.

ACKNOWLEDGMENTS

Melvin Z. Miquel is supported by the grant for fundamental research of the Next Generation Tatara Co-Creation Centre (NEXTA), which is established with Grant-in-aid for the Promotion of Regional Industries and University from Cabinet Office, Japan. Roger C. Reed is grateful to the Royal Academy of Engineering for the funding of a Research Chair.

COMPETING INTERESTS

On behalf of all authors, the corresponding author states that there is no conflict of interest.

OPEN ACCESS

REFERENCES

1. R.C. Reed: *The Superalloys: Fundamentals and Applications*, Cambridge University Press, Cambridge, 2006.
2. T.M. Pollock and S. Tin: Nickel-based superalloys for advanced turbine engines: chemistry, microstructure and properties. *J. Propuls. Power*, 2006, vol. 22, pp. 361–74.
3. B.H. Kear and H.G.F. Wilsdorf: Dislocation configuration in plastically deformed polycrystalline Cu_3Au alloys. *Trans. Metall. Soc. AIME*, 1962, vol. 224, pp. 382–86.
4. C. Carry and J.L. Strudel: Apparent and effective creep parameters in single crystals of a nickel base superalloy—II: secondary creep. *Acta Metall.*, 1978, vol. 26, pp. 859–70.
5. D. Barba, et al.: On the microtwinning mechanism in a single crystal superalloy. *Acta Mater.*, 2017, vol. 135, pp. 314–29.
6. B.H. Kear, J.M. Oblak, and A.F. Giamei: Stacking faults in gamma prime Ni_3(Al,Ti) precipitation hardened nickel-base alloys. *Metall. Trans.*, 1970, vol. 1, pp. 2477–86.
7. T. Clyne: Analysis of creep-dominated tensile stress-strain data. *Int. J. Mech. Sci.*, 2025, vol. 295, p. 110295.
8. Y.M. Wang-Koh, O.M.D.M. Messe, C.W.M. Schwalbe, C.N. Jones, and C.M.F. Rae: The effect of strain rate on the tensile deformation behavior of single crystal, Ni-based superalloys. *Metall. Mater. Trans. A*, 2023, vol. 54A, pp. 1456–68.
9. S. Utada, et al.: Tensile testing of Ni-based single crystal superalloys: what is the correct ''point of view''?, in *Superalloys 2024*. J. Cormier, et al. eds., Springer Nature Switzerland, Cham, 2024, pp. 427–38.
10. J. Blaber, B. Adair, and A. Antoniou: Ncorr: open-source 2D digital image correlation matlab software. *Exp. Mech.*, 2015, vol. 55, pp. 1105–22.
11. M. Feller-Kniepmeier, T. Link, I. Poschmann, G. Scheunemann-Frerker, and C. Schulze: Temperature dependence of deformation mechanisms in a single crystal nickel-base alloy with high volume fraction of γ' phase. *Acta Mater.*, 1996, vol. 44, pp. 2397–2407.
12. P.H. Thornton, R.G. Davies, and T.L. Johnston: The temperature dependence of the flow stress of the γ' phase based upon Ni3Al. *Metall. Trans.*, 1970, vol. 1, pp. 207–18.
13. D.M. Shah and D.N. Duhl: The effect of orientation, temperature and gamma prime size on the yield strength of a single crystal nickel base superalloy, in *Superalloys 1984 (Fifth International Symposium)*. TMS, 1984, pp. 105–14.
14. G.R. Leverant, M. Gell, and S.W. Hopkins: The effect of strain rate on the flow stress and dislocation behavior of a precipitation-hardened nickel-base alloy. *Mater. Sci. Eng.*, 1971, vol. 8, pp. 125–33.
15. R.R. Jensen and J.K. Tien: Temperature and strain rate dependence of stress-strain behavior in a nickel-base superalloy. *Metall. Trans. A*, 1985, vol. 16, pp. 1049–68.
16. W.W. Milligan and S.D. Antolovich: Yielding and deformation behavior of the single crystal superalloy PWA 1480. *Metall. Trans. A*, 1987, vol. 18, pp. 85–95.
17. J. Wang, W.-G. Guo, Y. Su, P. Zhou, and K. Yuan: Anomalous behaviors of a single-crystal Nickel-base superalloy over a wide range of temperatures and strain rates. *Mech. Mater.*, 2016, vol. 94, pp. 79–90.
18. E.F. Westbrooke, L.E. Forero, and F. Ebrahimi: Slip analysis in a Ni-base superalloy. *Acta Mater.*, 2005, vol. 53, pp. 2137–47.
19. P. Qu, et al.: Tensile deformation dominated by matrix dislocations at intermediate temperatures revealed using *in-situ* EBSD in superalloys. *Mater. Res. Lett.*, 2024, vol. 12, pp. 116–24.
20. H. Long, et al.: Shearing mechanisms of stacking fault and anti-phase-boundary forming dislocation pairs in the γ' phase in Ni-based single crystal superalloy. *J. Alloys Compd.*, 2017, vol. 724, pp. 287–95.
21. P. Zhang, et al.: Deformation modes in the single-crystal nickel-based superalloy CMSX-4 during compressive deformation at 1000 °C. *Metall. Mater. Trans. A*, 2022, vol. 53A, pp. 388–93.
22. Y.F. Liu, et al.: Dependence on temperature of tensile properties of the single-crystal superalloy DD11. *Mater. Sci. Technol.*, 2018, vol. 34, pp. 1188–96.
23. Z.H. Tan, et al.: Temperature dependence on tensile deformation mechanisms in a novel nickel-based single crystal superalloy. *Mater. Sci. Eng. A*, 2020, vol. 776, p. 138997.
24. Q. Ding, et al.: Temperature effects on deformation substructures and mechanisms of a Ni-based single crystal superalloy. *Appl. Mater. Today*, 2021, vol. 23, p. 101061.
25. R. Jiang, et al.: Strain accumulation and fatigue crack initiation at pores and carbides in a SX superalloy at room temperature. *Int. J. Fatigue*, 2018, vol. 114, pp. 22–33.
26. K. Liu, et al.: *In-situ* X-ray tomography investigation of pore damage effects during a tensile test of a Ni-based single crystal superalloy. *Mater Charact*, 2021, vol. 177, p. 111180.
27. S.X. Li and D.J. Smith: Temperature and orientation dependence of elastic and yield properties of single crystal nickel base superalloy. *Mater. Sci. Technol.*, 1995, vol. 11, pp. 1253–60.